Composites Science and Technology 219 (2022) 109236

Contents lists available at ScienceDirect

Composites Science and Technology

journal homepage: www.elsevier.com/locate/compscitech

Interlaminar and translaminar fracture toughness of Automated Manufactured Bio-inspired CFRP laminates

Verónica Rodríguez-García [a,c], M. Herráez [d], Vanesa Martínez [e], Roberto Guzman de Villoria [b,c,*]

[a] EIT Manufacturing West, S.L. Paseo de Mikeletegi 1, Donostia/San Sebastian, 20009, Gipuzkoa, Spain
[b] Department of Mechanical Engineering, Escuela Politécnica Superior de Zamora, University of Salamanca, Avenida Requejo, 33, 49022, Zamora, Spain
[c] FIDAMC, Foundation for the Research, Development and Application of Composite Materials, Avda. Rita Levi Montalcini 29, 28906, Getafe, Madrid, Spain
[d] Materials Science and Engineering Area, Escuela Superior de Ciencias Experimentales y Tecnología, Universidad Rey Juan Carlos, Madrid, Spain
[e] IMDEA Materials Institute, C/Eric Kandel, 2, 28906, Getafe, Madrid, Spain

ARTICLE INFO

Keywords:
Carbon fibre reinforced polymers
Bio-inspiration
Fracture toughness
Automatic tape lay-up
Prepreg

ABSTRACT

Natural structures such as nacre show an outstanding balance of strength and toughness, despite comprising mainly brittle constituents; this is a highly desirable combination of properties scarcely seen in synthetic composites. In this study, carbon fibre-reinforced polymer (CFRP) laminates mimicking the structure of nacre ('brick-and-mortar') were manufactured using the automated tape laying (ATL) technique, as a means of enhancing their interlaminar properties and fracture toughness. The interlaminar fracture toughness of the bio-inspired CFRP laminates was measured via double cantilever beam (DCB) and three-point bending end-notched flexure (3ENF) tests. The results indicated increments of up to 32% and 92%, respectively, in the interlaminar fracture toughness when compared with that of conventional continuous CFRP samples. In addition, the translaminar fracture toughness of the developed nacre-inspired CFRPs was measured through a compact tension (CT) test, which revealed increments of up to 30%. Finally, different reinforcement mechanisms were analysed to understand the effect of the 'brick-and-mortar' structure.

1. Introduction

The intrinsic layered nature of carbon fibre reinforced polymers (CFRPs) makes them prone to delamination failure and low fracture toughness, and these limit the full exploitation of these materials. Several strategies have been examined to improve the interlaminar properties and to reduce the sudden failure of CFRPs. These include the introduction of 3D fabrics [1], stitching [2], Z-pinning [3], adding micro/nanofillers to the interlaminar space of the composite material [4,5], and bio-inspiration [6].

Among the different strategies, mimicking biomaterials such as nacre, has emerged as an effective approach to enhance the mechanical behaviour of CFRP materials [7,8]. Nacre is composed of brittle aragonite platelets (95 wt %) embedded in an organic matrix in a structure also known as 'brick-and-mortar'. Nacre shows an outstanding fracture strength (3000 times greater) and toughness (20–30 times greater) than those of its main constituent [7–10]. This mechanical behaviour results from several toughening mechanisms, ranging from the nanoscale to the macroscale (multi-level hierarchy), acting in a cooperative manner [7,11,12]. The main energy dissipation mechanisms are platelet sliding [7,10,13,14], strain hardening [9,15], crack deflection and twisting [7,13,16], and platelet/brick pull-out [7,13,15].

To exploit these toughening mechanisms, the 'brick-and-mortar' structure of nacre has been replicated in a variety of constituent materials [7,8,10,11,13]. It has been shown that 'brick-and-mortar' CFRPs, with pseudo-ductile behaviour [6] and nonlinear response with warning before failure [17,18], can be obtained by introducing discontinuities in the CFRPs. Furthermore, the hierarchy levels can be optimised to tune the nonlinear mechanical response [19]. On the other hand, crack deflection and damage diffusion mechanisms have been exploited by introducing bio-inspired tiled-microstructures into CFRPs, thereby improving the fracture behaviour [15,20,21]. Different patterns of micro-cuts have also been implemented in CFRPs to enhance their translaminar fracture behaviour [22]. In addition, more complex biomimetic structures have been introduced in CFRPs. These include a crossed-lamellar microstructure similar to that of shells [23], or Bouligand structures found in the dactyl club of the mantis shrimp (stomapods); these reduce the impact damage in CFRPs [24–26].

* Corresponding author. EIT Manufacturing West, S.L. Paseo de Mikeletegi 1, Donostia/San Sebastian, 20009, Gipuzkoa, Spain.
E-mail address: roberto.guzman@usal.es (R. Guzman de Villoria).

https://doi.org/10.1016/j.compscitech.2021.109236
Received 28 May 2021; Received in revised form 9 November 2021; Accepted 19 December 2021
Available online 24 December 2021

As reported in most of the studies on bio-inspired CFRP manufacturing, the main drawbacks are that the process is carried out manually [6,17,18,21–23], and it is extremely time-consuming to produce large-scale composites for comprehensive mechanical characterisation of bio-inspired composites. Nevertheless, in a recent study, the authors developed a manufacturing technique for producing bio-inspired CFRP. It involves mimicking the structure of nacre, in a two-dimensional (2D) version, using automated tape laying (ATL) at 100% speed (12 m/min); the produced CFRP exhibits nonlinear behaviour when subjected to tensile tests [27].

In this study, the fracture toughness of bio-inspired nacre-like CFRPs manufactured using commercial materials and processes already implemented in the aerospace and automotive industries, such as ATL, was studied [27]. The double cantilever beam (DCB) and three-point bending end-notched flexure (3ENF) tests were carried out to analyse their interlaminar properties. In addition, a compact tension test was performed to study the translaminar fracture toughness of the CFRPs produced.

2. Materials and methods

2.1. Materials

The material used in this study is HexPly® 8552 unidirectional carbon fibre (AS4) prepreg from Hexcel (AS4 fibre density of 1.79 g/cm^3, 8552 resin density of 1.30 g/cm^3, fibre volume fraction of 59%, and nominal cured ply thickness of 0.184 mm) [28].

2.2. Manufacturing of bio-inspired laminates

A gantry ATL machine (MTorres; Figure 1 of the supplementary information (SI)) was used to manufacture 'brick-and-mortar' laminates (300 mm × 300 mm) with different fibre lengths (Fig. 1): 50, 25, and 10 mm (referred to in this article as 'Length50', 'Length25', and 'Length10' laminates, respectively). The ATL machine contains two knives that make controlled and continuous cuts perpendicular to the fibre direction following the 'brick-and-mortar' design (Fig. 1). At the same time, the ATL machine lays-up the cut plies over a flat metallic tool according to the selected stacking sequence [27]. The distance between the cuts was constant (fibre length, FL), and an overlapping region with a length of FL/2 between the even and odd plies was maintained (Fig. 1). Laminates without cuts were also made and used as a reference ('Continuous').

Following the lay-up process, the laminates were placed in a flat steel tool, and a vacuum bag was used (Fig. 2 of the SI) to cure them. Type-K thermocouples were placed on both the laminates and the tool to monitor the temperature. Finally, the laminates were cured in an autoclave according to the manufacturer's instructions (2 °C/min up to 180 °C followed by a plateau of 180 min at 180 °C and 100 psi). Details of the manufacturing process are described in a previous study [27].

For each configuration ('Length50', 'Length25', 'Length10', and 'Continuous'), several laminates with different stack-up sequences were manufactured, as can be observed in Fig. 3 of the SI (the sequence was defined according to test standards). Laminates with a stacking sequence of $[(0)_8/(0)_8]$ were produced to obtain DCB specimens. A 63 mm release film insert (25 μm thick) was carefully placed by hand in the midplane of the laminate. This release film served as the delamination initiator necessary for conducting the interlaminar fracture toughness test (Fig. 3a of the SI). Similarly, laminates with a stack-up sequence of $[(0)_9/(0)_9]$ and a 50 mm release film were manufactured for the 3ENF interlaminar fracture toughness test (Fig. 3b of the SI). In addition, laminates with a stack-up sequence of $[90(0/90)_{10}]_s$, in which 90° plies are continuous (without cuts), were manufactured to prepare CT specimens (Fig. 3c of the SI). To evaluate the quality of the manufacturing process, all laminates were inspected using ultrasonic immersion scanning (Tecnitest). Furthermore, the fibre void volume, fibre length, and gap length between the fibres for the $[(0)_8/(0)_8]$ and $[(0)_9/(0)_9]$ laminates were determined (Table 1 of the SI). Details of the process are described in section 1.2 of the SI and in another study [27].

2.3. Double cantilever beam test

DCB samples were manufactured and tested according to the ASTM D5528–01 standard [29]. Five samples were machined (25 mm × 150 mm, Fig. 3a of the SI) and piano hinges were bonded (Loctite 496) [29]. To follow crack growth during the test, the lateral sides of the specimens were sprayed with white paint, and every millimetre (up to 55 mm from the end of the insert) was marked with a black pen (Fig. 4 of the SI) [29]. The specimens were then mounted on a universal testing machine (Z01OTH from Zwick, load cell of 10 kN), and a precrack of 3–5 mm was created (1 mm/min). Subsequently, the machine was unloaded at a controlled velocity, and the test was carried out at 1 mm/min. Data were taken at the visual onset of the crack and every millimetre thereafter using a magnifying glass. The load, crack length, and arm displacement were recorded as a function of time [29,30]. This experimental

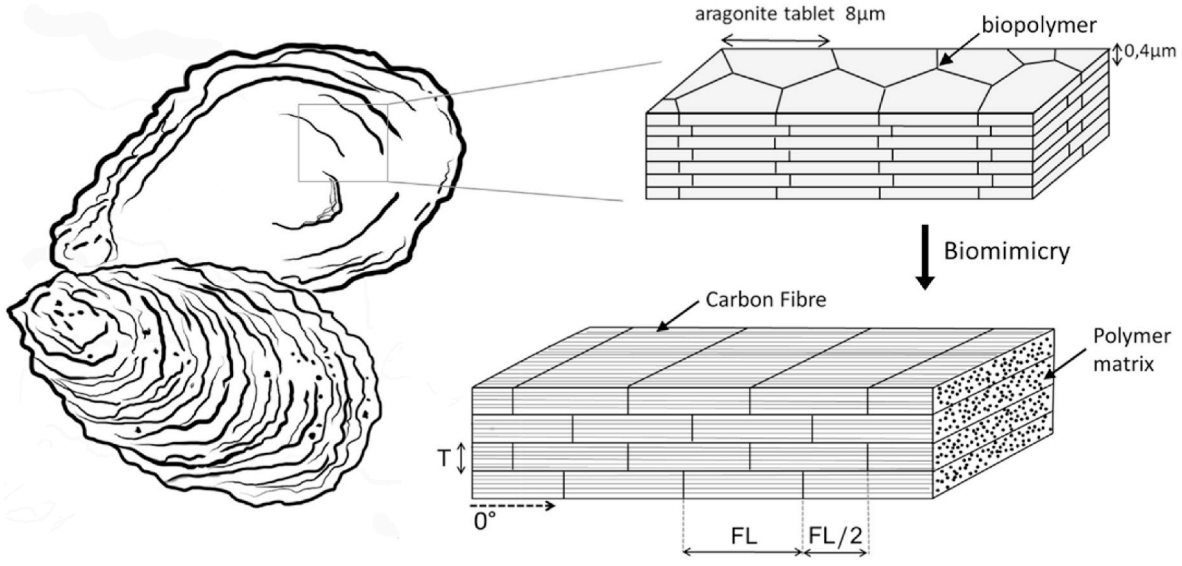

Fig. 1. 'Brick-and-mortar' arrangement of aragonite nanoplatelets found in the structure of nacre and biomimetic implementation in CFRP laminates. T stands for ply thickness and FL for fibre length.

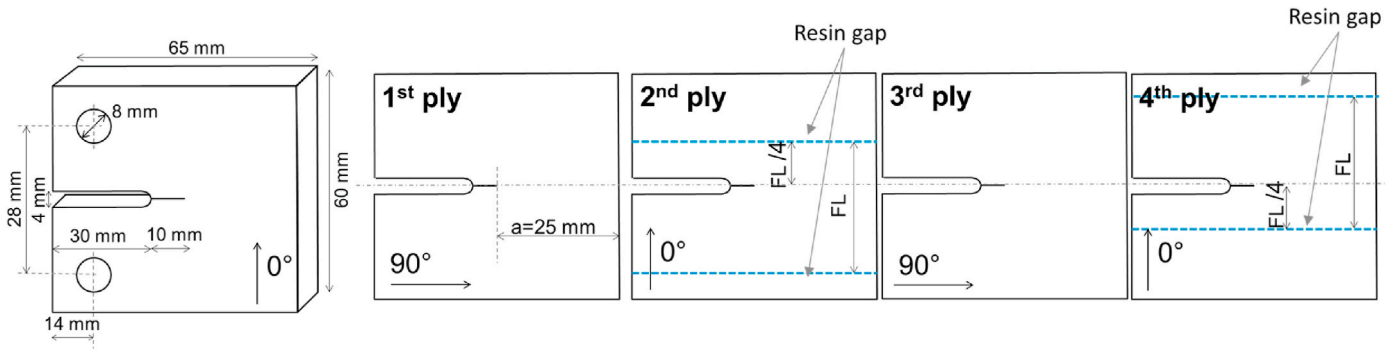

Fig. 2. Scheme of a compact tension (CT) specimen with a stack-up sequence of $[90/(0/90)_{10}]_s$ and an image of its first four plies. Even plies in the 90° direction are continuous plies, while odd plies in the 0° direction follow the 'brick-and-mortar' design. Dotted blue lines in the 0° plies indicate the location of the resin gap, where *FL* is the fibre length of the carbon fibre 'brick'.

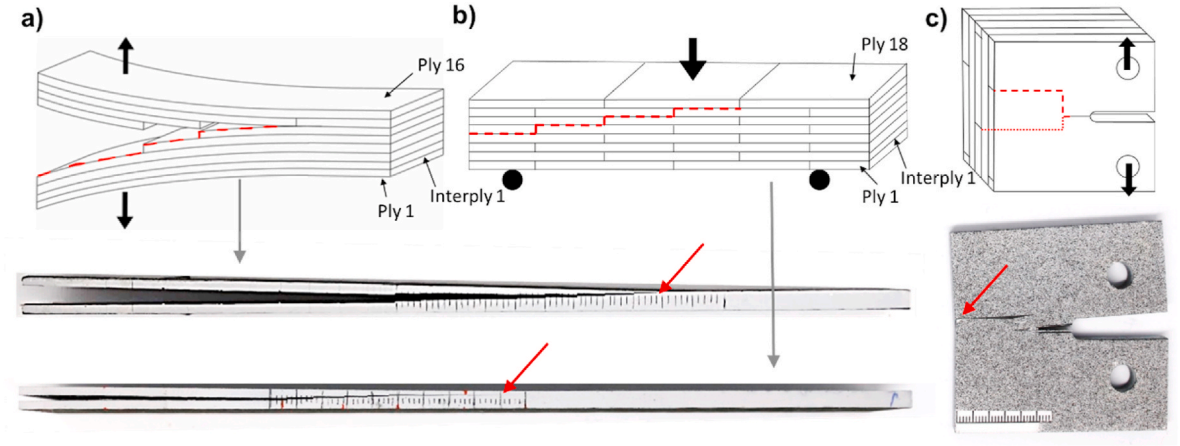

Fig. 3. Simplified scheme and optical picture of a 'Length10' specimen tested using (a) DCB, (b) End-notched flexure (ENF), and (c) CT tests. Dotted red lines indicate the crack path and the red arrows indicate the tip of the crack. Each painted mark on all of the specimens equals 1 mm. Schemes are not to scale and the numbers indicate the ply numbering used in this study, with the lower ply being considered to be the first.

Table 1
Average thickness (mm) and total interlaminar fracture toughness G_{DCB} (kJ/m^2) measured in 'Length50', 'Length25', 'Length10', and 'Continuous' laminates subjected to the DCB test for 50 mm of the crack length.

	Thickness (mm)	Initial location of the crack tip (# interply)	G_{DCB} (kJ/m^2)
Continuous	3.13 ± 0.04	8–9	0.27 ± 0.03
Length50	3.13 ± 0.02	8–9	0.300 ± 0.006
Length25	3.12 ± 0.02	8–9	0.329 ± 0.015
Length10*	3.12 ± 0.02	9–10	0.36 ± 0.03

* For 'Length10' samples, the test started with the crack tip at the 9th–10th interply. For rest of the samples, the crack tip was located at the midplane of the coupon (8th–9th interply) at the beginning of the test.

procedure has an associated considerable error, which has been calculated considering a precision of 0.2 mm when measuring crack growth. The tests were stopped when the crack reached approximately 50 mm from the end of the precrack [29]. The singular structure of the samples will lead to crack migration out of the midplane during the test and, thus resulting in different thicknesses of the arms of the specimens. Hence, it was not possible to use the calculation methods indicated in the standard procedure. Details regarding the calculation method are provided in the Experimental section.

The surfaces of the broken specimens were analysed using scanning electron microscopy (SEM, EVO MA 15 by ZEISS at an accelerating

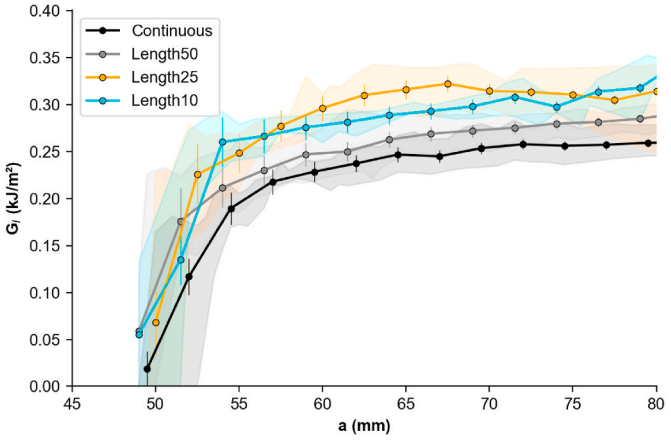

Fig. 4. Representative R-curve obtained from DCB tests on 'Length50', 'Length25', 'Length10' and 'Continuous' laminates. Bars indicate the error, considering a precision of 0.2 mm in the measurement of crack growth. The coloured regions indicate the deviation of the R-curves obtained for each configuration.

voltage of 15 kV), and the samples were sputtered with a thin layer of gold for 60 s at 35 mA (Quorum Q150 Rotary-Pump Sputter).

2.4. Three-point end-notched flexure test

Three-point end-notched flexure tests were performed based on the ASTM D7905 standard [31]. Four samples per laminate were machined (180 mm × 25 mm, Fig. 3b of the SI), painted, and marked using the same methodology as previously described for the DCB test (Fig. 5 of the SI). In this case, a 3–5 mm precrack was carefully cut by hand using a sharp knife. The samples were then mounted onto an Instron 3384 testing machine with a load cell of 2 kN. The precrack tip was placed 15 mm from the loading roller (Fig. 5 of the SI), and the tests were performed at 0.5 mm/min. Once the crack had progressed to a range of 10–15 mm, the sample was unloaded at 5 mm/min. After each load-unload cycle, the sample was shifted, leaving 15 mm between the crack tip and the roller to be loaded [32,33]. This load-unload process was repeated four times [34,35] (Fig. 6 of the SI). Data were collected at the visual onset of the crack for every millimetre of crack growth using a magnifying glass. The load, crack length, and arm displacement were recorded as a function of time [30,35]. Owing to the crack plane deflection during the test, the calculation method (details provided in the experimental section) differs from that of the method specified in the standard. Similar to the DCB coupons, the fracture surfaces of the samples tested were sputtered with a thin layer of gold and examined using a Helios Nanolab 600i SEM at 5 kV and 21 pA.

2.5. Compact tension test

In this study, the CT tests were performed on rectangular specimens (60 mm × 65 mm) with a stack-up sequence of $[90(0/90)_{10}]_s$, as defined by Pinho et al. [36,37]. A 30 mm long × 4 mm wide notch and two load-bearing holes (with 8 mm diameters) were machined in each specimen (Fig. 2). At the end of each notch, a 10 mm slit was machined using a standard wire-cutting machine (0.2 mm filament). The distance between the notch and the resin gap is FL/4 (Fig. 2). That is, for all 'Length50' coupons, the distance between the notch and the cut was 12.5 mm; for 'Length25' coupons this distance was 6.25 mm; and for 'Length10' the distance was 2.5 mm. According to these measurements, the Length50 specimens contain only one cut in each 0-ply, thus leading to a less representative volume of the microstructure. However, the critical length calculation shows that this microstructure should not lead to pull-out, even if a larger specimen is used (section 3.4).

A speckled pattern was created on the surface of the specimen to identify any surface damage or highly deformed regions produced during the test. For each laminate, five specimens were tested using an Instron 3384 testing machine (load cell of 10 kN, 0.5 mm/min) (Fig. 7 of the SI) to reach a crack growth of approximately 25 mm. A high-resolution charge-coupled device (CCD) camera was used to record the results. Digital image correlation (DIC) was used to analyse the surface of the sample by counting pixels [37]. Details of the calculation method are provided in the experimental section.

3. Results and discussion

All the ultrasonic C-scan images showed no voids, ply delamination, or defects. In Fig. 8 of the SI, it can be appreciated how the gaps created during the manufacturing process, between the cut fibres, were filled with resin, thus producing resin pockets [27]. Furthermore, the fibre and gap length distribution results are shown in section 2.1 of the SI. Regarding FL, a deviation of approximately 2 mm was observed in all the 'brick-and-mortar' laminates, and this is related to the precision of the ATL [27] (Fig. 9a of the SI). The average gap length for all the 'brick--and-mortar' laminates was 34–90 μm (Fig. 9b of the SI), which is similar that reported in a previous study conducted using the same ATL machine [27]. No significant differences in fibre (standard deviation, 1.5%) or void volume (*ca.* 0%) were found among the laminates manufactured (Table 1 of the SI).

3.1. Calculation method

The tested 'brick-and-mortar' specimens were not symmetrical with respect to the crack plane because of crack migration during the fracture process. The tested DCB specimens showed two arms with different thicknesses along the longitudinal direction of the specimen. In addition, the cracks observed in the 3ENF specimens were deflected to the upper layers during their propagation. Regarding the CT samples, several cracks appeared in the outer ply, as shown in Fig. 3.

The standard calculation methods [29,31] indicated that symmetrical specimens with a single crack front could not be applied to our 'brick-and-mortar' test. In addition, the DCB [38–40] and end-notched flexure (ENF) [41–43] methods developed for asymmetrical specimens could not be applied to these 'brick-and-mortar' specimens, as the position of the crack plane varied during the test. Regarding the CT test, the usual data reduction methods for the translaminar fracture toughness [37,44–46] require the observation of a single crack. However, several crack fronts were present in the specimens during the tests performed in this study; thus, these methods could not be applied as well.

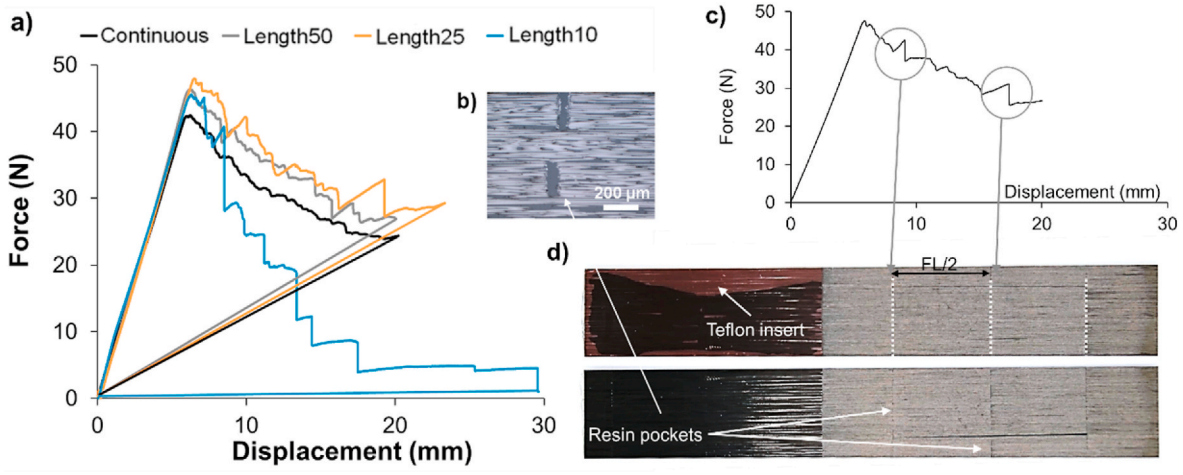

Fig. 5. (a) Representative *force vs displacement* curves; (b) cross section of resin pockets; (c) association of the force vs displacement curve obtained for a 'Length50' coupon when subjected to a Mode I interlaminar fracture toughness test with (d) the broken specimen load drops match with resin pockets created in the gaps between the cut fibres.

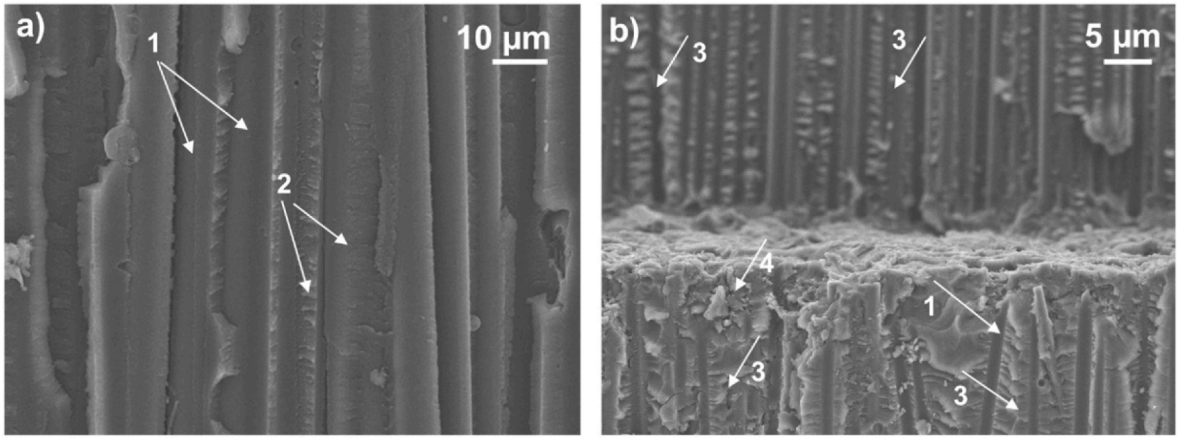

Fig. 6. Scanning electron microscopy (SEM) images of the fracture surfaces, (a) 'Continuous' (× 1000), and (b) 'Length10' (× 500) laminates, when subjected to DCB tests. Arrows labelled with: the number 1 show the fibre imprint; number 2 arrows the riverlines; and number 3 arrows the shallow cusps.

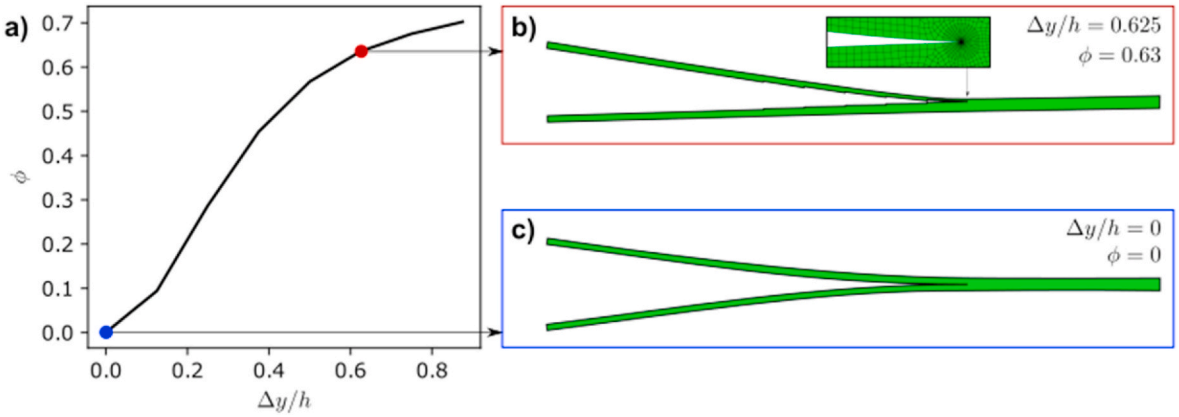

Fig. 7. (a) Mixed mode ratio vs. relative vertical offset of the cracking plane, and overview of an FE model with (b) $\Delta y/h = 0.63$ and (c) $\Delta y/\ h = \ 0$.

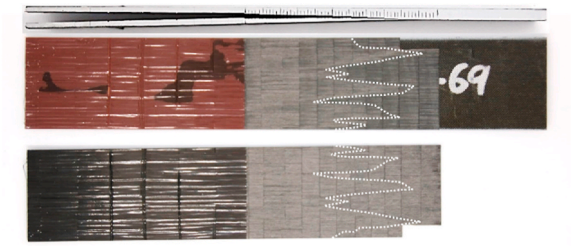

Fig. 8. Detailed failure mode of 'Length10' laminates. Dotted lines indicate the crack fronts.

The area method, based on the calculation of the area of the load-displacement curve divided by the area of the crack created, permitted the toughness of conventional bio-inspired composites to be quantitatively measured [47–50]. This was also the same for the CFRPs in Mode I [51–54], Mode II [32,53,55], and CT [37,45,46] tests. In this study, the area method was used to estimate the interlaminar fracture toughness of the samples subjected to the DCB and 3ENF tests and the translaminar fracture toughness of the samples subjected to the CT tests (denoted as G_{DCB}, G_{3ENF}, and G_{CT}, respectively) for both continuous and discontinuous specimens. For G_{DCB}, a crack length of approximately 50 mm was analysed. In addition, the R-curve of DCB samples was obtained using this method and by assuming a linear-elastic behaviour (straight unload and zero offset) to calculate the area between each crack increment of the R-curve [56,57] for the first 30 mm of crack growth. It is assumed that this method has an associated error that is calculated as it neglects any plastic or friction effects. This same assumption was applied to calculate the G_{CT} [37]. Details of the method are shown in Fig. 10 of the SI.

3.2. Double cantilever beam test

The results of the DCB tests are shown in Table 1. Specimens 'Length50', 'Length25', and 'Length10' exhibited 10%, 20%, and 32% higher G_{DCB}, respectively, compared to that of the 'Continuous' samples. In all the samples, the crack growth reached approximately 50 mm. It should be noted that during the precracking process of the 'Length10' laminates, the crack tip deflected from the midplane (8th–9th interply, Fig. 3) to the 9th–10th interply (Fig. 3) owing to the short overlap length (5 mm, FL/2). Because several crack deflections were produced in each sample, the initial effect mentioned with respect to sample 'Length10' may not influence the toughness of the material significantly.

In contrast, the R-curves (Fig. 4) showed higher fracture toughness values for the 'brick-and-mortar' coupons along the propagation of the entire crack. The G_I error was calculated and included in the R-curve, and it was observed that this measurement was reliable for the propagation area of the curve (Fig. 4). As shown in Fig. 5, the gap between the cut fibres was filled with resin during the manufacturing process, thereby creating resin pockets [27].

The results showed that the increase in fracture toughness increased with the increasing number of resin pockets met by the crack.

With respect to the force and displacement curves, 'Continuous' coupons showed a typical CFRP Mode I curve (Fig. 5a), which indicates

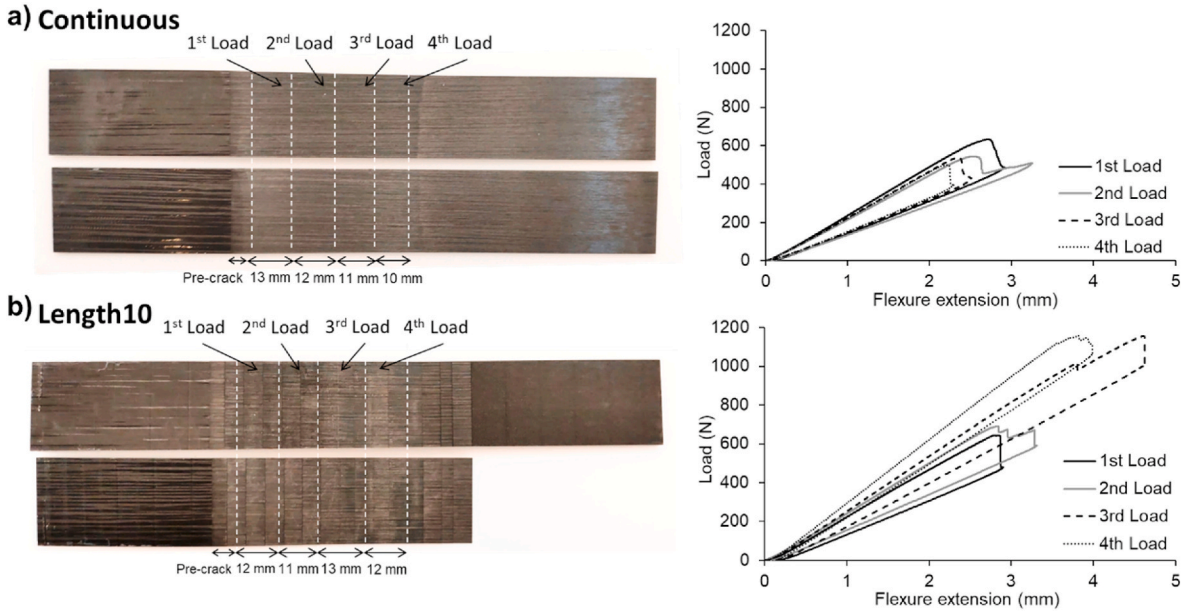

Fig. 9. The tested (a) 'Continuous' and (b) 'Length10' samples subjected to four load-unload cycles and their representative *load vs displacement* curves obtained by applying the 3ENF test. White dotted lines indicate the beginning and end of each load cycle performed on that sample with the corresponding crack length indicated. 'Length10' picture shows cuts mainly located between starting and ending points of the loading cycle, thus leading to a more progressive damage process. However, it can be seen that the beginning third load cycle coincides with a cut, and this leads to a more abrupt load drop.

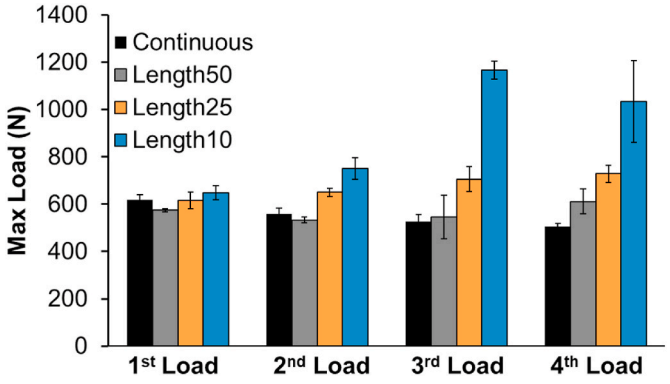

Fig. 10. Average maximum load obtained in Mode II tests for each load step and for each of the laminates: 'Continuous', 'Length50', 'Length25', and 'Length10'.

stable and continuous crack growth along the specimen [29]. The typical features of a Mode I fracture, such as fibre imprint, broken fibres [58,59], and riverlines [58–60], were observed using SEM (Fig. 6a). Fibre bridging was scarcely observed in either the continuous or discontinuous samples.

Additionally, the 'brick-and-mortar' coupons showed stick-slip-type curves (Fig. 5a) [52]. It has been reported that resin pockets arrest crack propagation by crack blunting, which leads to enhanced fracture toughness [61]. The resin pockets located between the cut fibres acted as crack arresters, thus increasing the load necessary for crack propagation. This was followed by sudden crack propagation and a subsequent load drop [20,60,62] (Fig. 5b, c, and d). This produces consistent stick-slip type curves (Fig. 11 of the SI) in the 'Length50' and 'Length25' laminates. The 'Length10' laminates show less consistent load drops associated with the less precise location of the cuts due to machine precision (Fig. 9 of the SI).

It was also possible for the crack to be deflected upward to the next interply when it reached a resin pocket (Fig. 6b). This process was observed throughout the different plies as the crack tip progressed (Fig. 5c and d). The crack deflection mechanism produced a tortuous path and a reduction in the stress intensity field locally experienced at the crack tip [63–65]; this also resulted in greater sample toughness.

Finally, during the tests, the thicknesses of the arms of the specimens varied as the cracks propagated and deflected, thus resulting in an asymmetric test (Fig. 3). The asymmetry in the DCB test produced a mixed-mode (Mode I and II) state at the crack tip while maintaining predominantly Mode I [38,66–68]. Within this asymmetrical condition, the failure mode varied during the test and increased the contribution of Mode II when the difference between the thicknesses of the arms increased [39,67]. Because of this contribution, shallow cusps were present on the fracture surface of the 'brick-and-mortar' specimens (Fig. 6b) [58,69]. Furthermore, there was a localised increase in the amount of matrix fracture per unit surface area, and this increased the overall toughness of the specimens [58,59,70].

The contribution of Mode II in the DCB tests was numerically estimated using the finite element (FE) model developed in Abaqus. The fracture surface observed in the experiments, following a stair-like pattern due to successive crack migrations, was explicitly represented in the numerical model to ascertain the effect of the geometrical features. The whole coupon was modelled using a homogenised single-material linear elastic solid, neglecting the local variability of the microstructure. Thus, the resin-rich regions were not represented. The mode mixity, defined as $\varphi = \frac{K_{II}^2}{K_I^2+K_{II}^2}$, was calculated at the crack tip based on the computation of the stress intensity factors K_I and K_{II} according to the global axis directions. The crack tip is located at a distance FL/2 from the latest crack migration, as shown in Fig. 7b, and is assumed to propagate in the horizontal direction (also detailed in Fig. 16b of the SI). A batch of FE models with increasing distance between the plane of the crack tip and the midplane of the coupon, Δy, were analysed, and the results are shown in Fig. 7. Here, the increment of mode mixity (φ) is evidenced by increasing $\Delta y/h$, where $2h$ is the coupon thickness and Δy is the distance in the through-the-thickness direction from the crack tip to the midplane of the coupon, as illustrated in Fig. 16 of the SI. As expected, when there was no offset from the midplane, $\Delta y = 0$; the DCB test exerted a pure opening fracture mode at the crack tip, and $\varphi = 0$. In contrast, when the delamination plane was away from the coupon

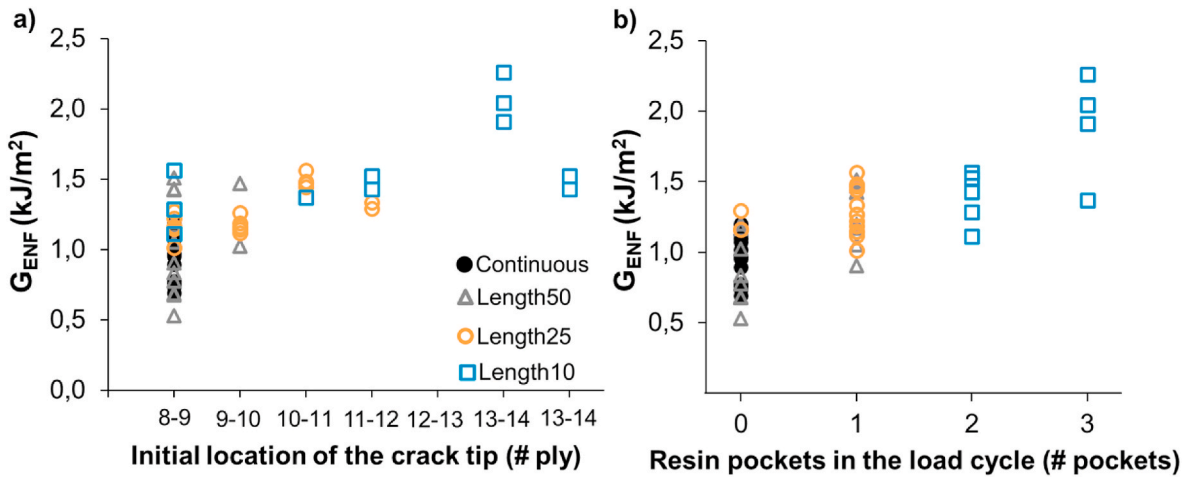

Fig. 11. (a) G_{ENF} vs Ply number in which each load cycle starts for each coupon tested. Since the crack is located between two plies, the crack ply is indicated as the carbon layer placed on the bottom of the crack (#ply). (b) G_{ENF} vs Number of resin pockets contained within the area analysed in the corresponding load cycle for each coupon tested. With respect to the ply numbering, ply 1 is considered to be the one touching the rollers while ply 18 is the one touching the load point, with the stacking sequence $[0_9/0_9]$.

midplane, the mismatching bending stiffness of the DCB arms introduced a non-negligible fracture Mode II contribution along the crack propagation.

A detailed description of the FE model (i.e., mesh, boundary conditions, material properties, etc.) can be found in section 3 of the SI.

Finally, as can be observed in Figs. 8 and 12 of the SI, for the 'Length25' and 'Length10' laminates, several crack fronts were created. The observed decomposition of the fracture process in several planes can also lead to an increase in resistance to crack growth [70].

These toughening mechanisms (resin pockets acting as crack arresters, crack deflection, mixed mode, and fracture decomposition) are in good agreement with the observed results (Table 1). The shorter the length of the fibre along the ply, the larger the number of cuts within the laminate. Therefore, more resin pockets tended to arrest the fracture process by increasing the tortuosity of the crack path (Fig. 12 of the SI). This, in turn, resulted in greater asymmetry and Mode II contribution, and thus a higher R-curve plateau [64] in comparison to the flat R-curve observed for the 'Continuous' plies (Fig. 4).

3.3. Three-point end-notched flexure test

The resulting curves of the specimens subjected to four load-unload cycles during the 3ENF tests [32,33] are presented in Fig. 9. The average maximum force reached during the test (Fig. 10) increased with the number of resin pockets. In general, higher values were observed for those 'brick-and-mortar' laminates with shorter fibre lengths: 18% and 60% increments were obtained between the first and the fourth cycle, for 'Length25' and 'Length10' laminates, respectively.

Regarding the G_{ENF} determined in each load cycle, the values also increased with the number of resin pockets contained in the coupon (Table 2). Furthermore, while the G_{ENF} values remained constant for the 'Continuous' samples along the four load cycles, the G_{ENF} values obtained for the 'brick-and-mortar' laminates increased with the number of load cycles. For example, for the 'Length10' laminates, an increment of 69% was observed between the 1st and 3rd load cycles.

Similar to the DCB coupons, the resin pockets acted as crack arresters in the 'brick-and-mortar' specimens. Once the crack reached a resin pocket, it deflected to the upper layer (Fig. 3). These crack arrester and

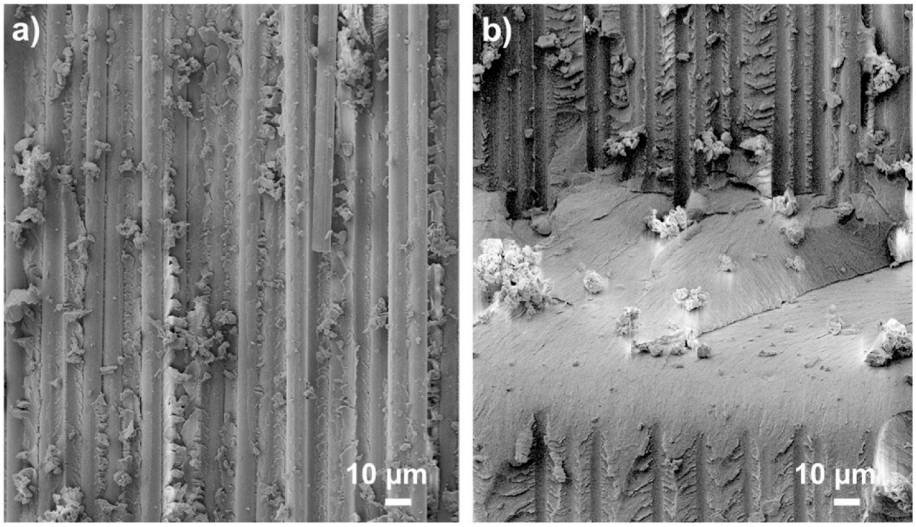

Fig. 12. SEM pictures (× 500) of the fracture surfaces obtained in the first cycle load in (a) 'Continuous' and (b) 'Length10' laminates subjected to a 3ENF test. Resin-rich areas in 'Length10' coupon correspond to the resin gap created between the cut fibres, where the crack deflected (the ply in the upper part of the picture is a different ply than the ply in the bottom part of the picture).

Table 2
Average thickness (mm) and average fracture toughness (kJ/m^2) obtained after each load-unload cycle ($G_{ENF\text{-}1st\ load}$, $G_{ENF\text{-}2nd\ load}$, $G_{ENF\text{-}3rd\ load}$, and $G_{ENF\text{-}4th\ load}$) for the four types of laminates subjected to the 3ENF test: 'Continuous', 'Length50', 'Length25', and 'Length10'.

	Thickness (mm)	$G_{ENF\text{-}1st\ load}$ (kJ/m^2)	$G_{ENF\text{-}2nd\ load}$ (kJ/m^2)	$G_{ENF\text{-}3rd\ load}$ (kJ/m^2)	$G_{ENF4th\ load}$ (kJ/m^2)
Continuous	3.13 ± 0.04	1.13 ± 0.06	1.0 ± 0.2	0.9 ± 0.2	0.89 ± 0.09
Length50	3.13 ± 0.02	1.3 ± 0.3	0.9 ± 0.2	1.0 ± 0.4	1.2 ± 0.2
Length25	3.12 ± 0.02	1.14 ± 0.09	1.19 ± 0.05	1.33 ± 0.05	1.41 ± 0.04
Length10	3.121 ± 0.011	1.3 ± 0.2	1.46 ± 0.08	2.2 ± 0.2	1.5 ± 0.1[a]

[a] Data from two coupons. The other two coupons broke during the fourth load cycle.

crack deflection effects led to increased interlaminar fracture toughness [61,64,67,71].

Moreover, owing to the deflection process, the crack tip was not located in the sample ply at the beginning of each load cycle (Fig. 11a). Moreover, these toughening mechanisms depend on the number of resin pockets reached by the crack during the test. The laminates with shorter fibre lengths (higher number of resin pockets) presented higher G_{ENF} values, as shown in Fig. 11b. However, since the crack only grew 10–15 mm in each test cycle, for coupons 'Length50' and 'Length25' the crack either did not pass through a resin pocket or only passed through one (Fig. 11a). Therefore, since just a few resin pockets were reached by the crack tip, slight increments were only produced in the 'Length50' laminates. A similar behaviour was found in the first and second load cycle for the 'Length25' laminates. In contrast, in the 'Length10' laminates, the crack propagated across several resin pockets, thus leading to greater toughness, as can be seen in Fig. 11b.

Crack deflection can be observed in the fracture surfaces of 'brick-and-mortar' specimens (Figs. 9, 12b and 14 of the SI), in contrast to the conventional delamination failure along the midplane of the 'Continuous' coupons (Figs. 9 and 12a). The contribution of Mode II was clearly observed in all the fracture surfaces in the form of shallow cusps [42] (Fig. 12).

Once the crack tip had migrated from the midplane to the upper layers of the specimen (Fig. 11a), the critical load for continuing crack propagation progressively increased, as shown in Fig. 10. A numerical FE model was built in Abaqus to study the influence of the relative position of the delamination plane along the coupon thickness on the stress intensity factors (K_I and K_{II}) at the crack tip in the 3ENF tests. The results from this model were compared with a reference configuration whose crack tip was located at the midplane of the coupon thickness (reference in Fig. 13). The results showed that the stress intensity factor K_{II} decreased as Δy increased when compared to the reference for the same applied load. This could be explained by the larger bending stiffness of the arms of the 3ENF coupon when $\Delta y/h$ increases. The minimum bending stiffness of the arms occurs for $\Delta y = 0$, with $I_t = I_1 + I_2 = \frac{1}{6}bh^3$. In contrast, as the delamination plane moved further away from the midplane of the coupon, the bending stiffness of the arms was higher: $\lim_{\Delta y \to h} I_t = \frac{2}{3}bh^3$, which was four times larger than that of $\Delta y = 0$ (see section 2.4 and Fig. 13 of the SI). Although these estimates of the moments of inertia assume the sections of the arms to be uniform and do not follow a progressive stair-like fashion, these results explain the higher loads required for crack propagation after successive load cycles, as previously shown in Fig. 9. Moreover, mode mixity φ, was found to be independent of the position of the delamination plane (Fig. 13). Therefore, pure Mode II fracture was reported, regardless of $\Delta y/h$.

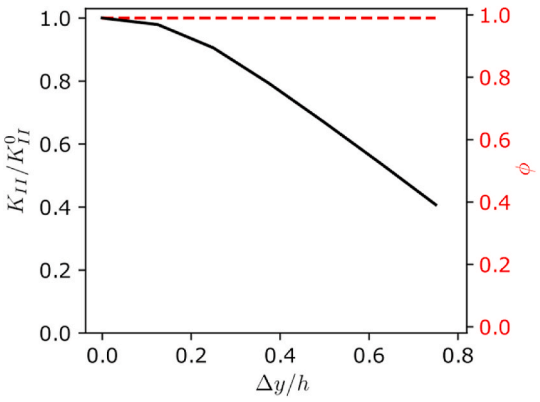

Fig. 13. Influence of the relative position of the delaminating plane: relative stress intensity factor in Mode II in the numerical model of the ENF test for the same applied load (solid black line), and mixed mode ratio (dashed red line).

A detailed description of the FE model (i.e., mesh, boundary conditions, material properties, etc.) can be found in section 3 of the SI.

3.4. Compact tension test

The representative *load vs. displacement* curves obtained via the CT tests are shown in Fig. 14a. 'Continuous', 'Length50', and 'Length25' laminates show typical 'stick and slip'-type curves associated with unstable crack propagation [37,45]. However, the curves of 'Length10' laminates show a smoother curve, indicating that the crack growth behaviour was stable.

The translaminar fracture toughness (G_{CT}) results are shown in Fig. 14b. 'Length50', 'Length25', and 'Length10' laminates showed increments of 19%, 13%, and 29%, respectively, compared to that of the 'Continuous' laminates. Owing to the fibre configuration of the specimens, these fracture toughness values can be interpreted as Mode I critical energy release rate for fibre fractures in the 0° plies (parallel to the load direction) and the critical energy release rate for matrix crack propagation in the 90° plies (perpendicular to the load direction) [36]. In this study, since the 90° plies are continuous in all the laminates, any increment observed would be associated with the difference in the coupons with 0° discontinuous carbon fibre plies (the ones containing cuts, Fig. 2).

Fig. 15 shows the fracture surfaces of the specimens tested. 'Continuous' and 'Length50' samples showed small fibre bundles pull-out in the 0° plies (Figs. 15a and 12b). This is probably caused by translaminar fibre tensile failure of the continuous plies [46]. This behaviour is in good agreement with the 'stick and slip'-type curves observed in the 'Continuous' and 'Length50' samples, since large load drops correspond to an increase in crack propagation [37]. The Length25′ fracture surfaces also showed a few fibre bundles (Fig. 15c). However, 'Length25' specimens showed pull-out at ply-level in some of the fragments, approximately 6.2 mm long (which, in turn, is approximately FL/4, Fig. 2), and ply thickness. Pull-out at ply-level can be also clearly observed for 'Length10' laminates, with several 2.5 and 7.5 mm long fragments, which correspond to FL/4 and 3FL/4, respectively (Fig. 15d).

The following simple analytical model can be used to determine the critical ply length (L_{CT}) that prompts either fibre tensile failure or ply pull-out:

$$\sigma_{UT-fibre} \cdot w \cdot T = 2\tau \cdot (w + t) \cdot L_{CT},$$

where $\sigma_{UT-fibre}$ is the ultimate tensile strength of the fibre (*ca.* 1850 MPa [72]), τ is the interface shear strength (*ca.* 85 MPa [73]), w is the characteristic distance in the direction of the crack propagation, and t represents the ply thickness (0.184 mm). If $w \gg t$ the expression is written as:

$$\sigma_{UT-fibre} \cdot T \approx 2\tau \cdot L_{CT}.$$

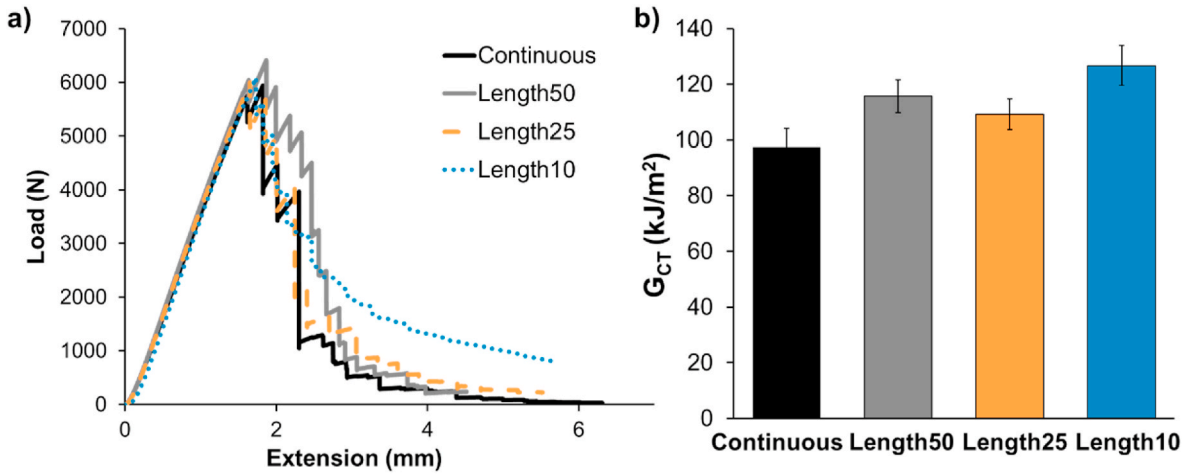

Fig. 14. (a) Representative Load vs Extension curve and (b) average translaminar fracture toughness values obtained from the CT tests using 'Continuous', 'Length50', 'Length25', and 'Length10' laminates.

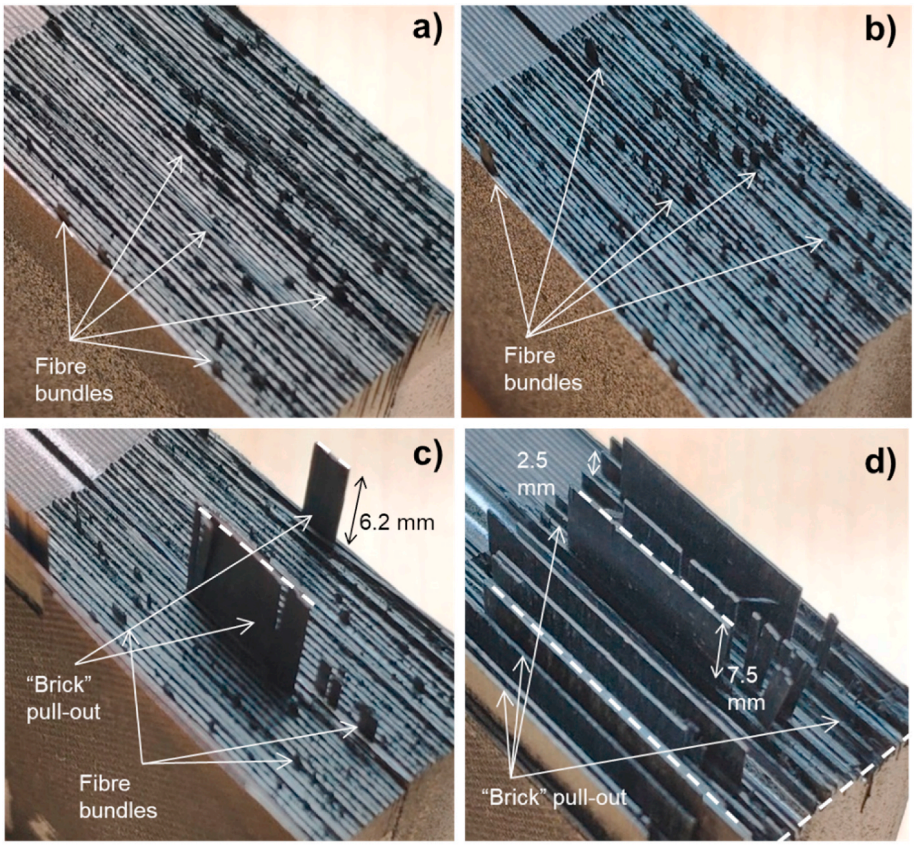

Fig. 15. Representative failure modes obtained when (a) 'Continuous', (b) 'Length50', (c) 'Length25' and, (d) 'Length10' laminates were subjected to the CT test.

Therefore, the critical length is obtained as:

$$L_{CT} \approx \frac{\sigma_{UT-fibre} \cdot T}{2\tau} = 2\ mm.$$

Considering this value, it was shown that the shorter distance between the resin gap and the notch in 'Length10' coupons (FL/4 = 2.5 mm, Fig. 2), which is of the order of L_{CT}, caused the crack to deflect, thus resulting in a higher amount of ply pull-out ('brick' pull-out). The 'brick' pull-out of the carbon fibre plies led to an increment in the toughness G_{CT} (Mode I fracture toughness in the in-plane direction) by the energy dissipation resulting from debonding and friction [74,75]. Simultaneously, this resulted in a more stable crack propagation, as shown in Fig. 14a [22,75]. Finally, the load in 'Length10' coupons (Fig. 14a) does not fall to zero as the pull-out process of the 7.5 mm long fragments cannot be completed, thereby transferring some stresses through friction.

In contrast, the carbon fibres for 'Continuous', 'Length50' and 'Length25' laminates were long enough to transfer stress from the matrix to the fibre via the interface, and this resulted in fibre tensile failure (Fig. 15). Due to this different behaviour, the load-extension curves (Fig. 14) and failure mode of these three samples (Fig. 15) are clearly different from those of the 'Length10' samples.

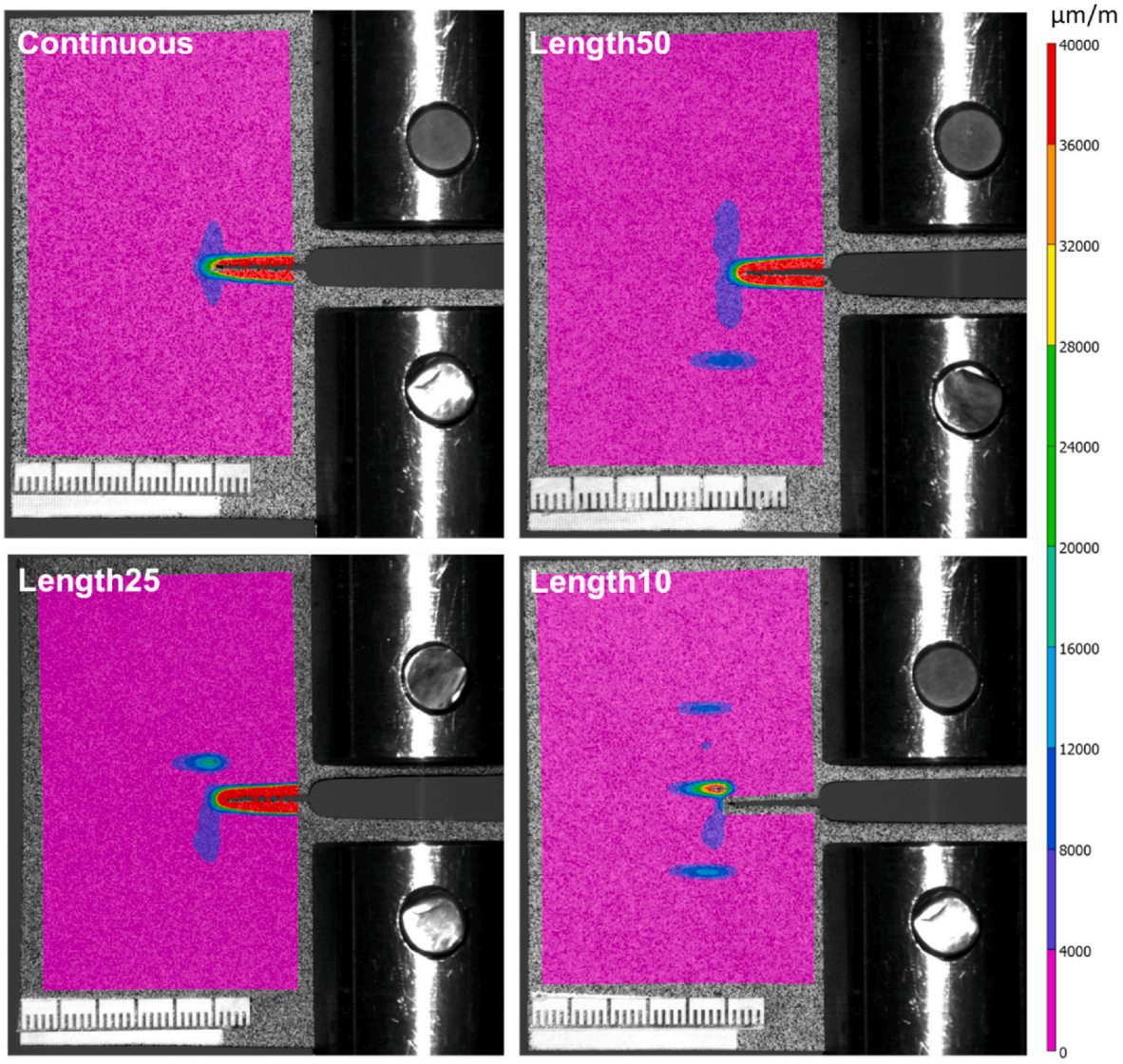

Fig. 16. Using digital image correlation (DIC), the longitudinal distribution of the strain (ε_{yy}) at the point of maximum load observed in 'Continuous', 'Length50', 'Length25', and 'Length10' laminates subjected to the CT test.

The DIC analysis performed during the CT tests showed varying strain distributions for the different laminates studied and a larger damaged area for the 'brick-and-mortar' laminates. Fig. 16 shows the longitudinal strains (ε_{yy}) at the point of maximum load (immediately before crack growth). It can be observed that the areas near the resin pockets in the 'brick-and-mortar' laminates were under a greater amount of strain, which led to the formation of multiple crack fronts in the outer layer (Figs. 3c and 15 of the SI).

Based on the above results, it has been shown that several mechanisms are at play in the 'brick-and-mortar' laminates. Apart from the fibre breakage and pull-out mechanisms of a conventional laminate, 'brick-and-mortar' laminates exhibit delamination of the fibre fragments cut by the ATL. In addition, several cracks were present during the mechanical tests but were only visible in the outer layer.

4. Conclusions

Bio-inspired CFRP laminates, mimicking the structure of nacre in a 2D version with different stacking sequences, were manufactured using ATL and autoclave curing to enhance their delamination properties. Interlaminar fracture toughness was determined by conducting DCB and 3ENF tests, and the translaminar fracture toughness was characterised using the compact tension test. All values were estimated using the area method.

The results of the DCB and 3ENF tests revealed that the interlaminar fracture toughness increased by 24% and 92% in the 'Length25' and 'Length10' laminates, respectively. In the DCB and 3ENF coupons, resin pockets act as crack arresters, and crack deflection produces a shielding effect that augments the fracture toughness. In addition, for the DCB coupons, the asymmetry produced due to crack deflection led to a Mode II contribution.

In this study, we have shown that the translaminar fracture toughness in the 'Length10' laminates was increased by up to 29% and that 'Brick' pull-out was observed in laminates 'Length25' and 'Length10', whose fracture toughness was greater due to energy dissipation caused by debonding and friction. In addition, this study has shed light on how the length and shape of the cuts can be optimised [22]. However, these processes cannot be implemented using an ATL machine.

In summary, this study has provided promising results, where the properties of fracture behaviour and fracture toughness have been enhanced by introducing a 'brick-and-mortar' structure into CFRPs produced using processes, materials and standards, such as ATL, that are currently being implemented in the aerospace industry.

Author statement

The authors Verónica Rodríguez-García and Roberto Guzmán de Villoria certify that all authors have seen and approved the final version of the manuscript being submitted. We warrant that the article is the authors' original work, hasn't received prior publication and isn't under consideration for publication elsewhere.

Declaration of competing interest

The authors declare that they have no known competing financial interests or personal relationships that could have appeared to influence the work reported in this paper.

Acknowledgements

The authors of this paper would like to thank L. C. Herrera-Ramírez, J.L. Jiménez, C. Vasquez, and M. Castillo for the preliminary results obtained during this project. We would also like to thank J. Mielgo for his help with the ATL programming, M. García with the ATL operating, and M. López for his assistance with the sample preparation. R. Guzman de Villoria was financially supported through a Beatriz Galindo fellowship (BEAGAL18/00091) awarded by the Spanish Ministry of Education, Culture and Sports, the Spanish Ministry of Economy and Competitiveness (Project BIOINSP-CFRP, PID2020-119003 GB-I00), and the University of Salamanca, program C1.

Appendix A. Supplementary data

Supplementary data to this article can be found online at https://doi.org/10.1016/j.compscitech.2021.109236.

References

[1] L. Tong, A.P. Mouritz, M.K. Bannister, 3D Fibre Reinforced Polymer Composites, Elsevier Science Ltd, 2002.
[2] D. Shu, Y.-W. Mai, Effect of stitching on interlaminar delamination extension in composite laminates, Compos. Sci. Technol. 49 (1993) 165–171, https://doi.org/10.1016/0266-3538(93)90056-M.
[3] M. Pankow, A. Salvi, A.M. Waas, C.F. Yen, S. Ghiorse, Resistance to delamination of 3D woven textile composites evaluated using End Notch Flexure (ENF) tests: experimental results, Composer Part Appl. Sci. Manuf. 42 (2011) 1463–1476, https://doi.org/10.1016/j.compositesa.2011.06.013.
[4] V. Dikshit, S. Bhudolia, S. Joshi, Multiscale polymer composites: a review of the interlaminar fracture toughness improvement, Fibers 5 (2017) 38, https://doi.org/10.3390/fib5040038.
[5] T.K. Tsotsis, Interlayer toughening of composite materials, Polym. Compos. 30 (2009) 70–86, https://doi.org/10.1002/pc.20535.
[6] R. Malkin, M. Yasaee, R.S. Trask, I.P. Bond, Bio-inspired laminate design exhibiting pseudo-ductile (graceful) failure during flexural loading, Composer Part Appl. Sci. Manuf. 54 (2013) 107–116, https://doi.org/10.1016/j.compositesa.2013.07.008.
[7] W. Huang, D. Restrepo, J. Jung, F.Y. Su, Z. Liu, R.O. Ritchie, J. McKittrick, P. Zavattieri, D. Kisailus, Multiscale toughening mechanisms in biological materials and bioinspired designs, Adv. Mater. 31 (2019) 1901561, https://doi.org/10.1002/adma.201901561.
[8] G.M. Luz, J.F. Mano, Biomimetic design of materials and biomaterials inspired by the structure of nacre, Philos. Trans. R. Soc. Math. Phys. Eng. Sci. 367 (2009) 1587–1605, https://doi.org/10.1098/rsta.2009.0007.
[9] R. Rabiei, S. Bekah, F. Barthelat, Failure mode transition in nacre and bone-like materials, Acta Biomater. 6 (2010) 4081–4089, https://doi.org/10.1016/j.actbio.2010.04.008.
[10] H.D. Espinosa, J.E. Rim, F. Barthelat, M.J. Buehler, Merger of structure and material in nacre and bone – perspectives on de novo biomimetic materials, Prog. Mater. Sci. 54 (2009) 1059–1100, https://doi.org/10.1016/j.pmatsci.2009.05.001.
[11] A.R. Studart, R.M. Erb, R. Libanori, Bioinspired hierarchical composites, in: C.-S. Kim, C. Randow, T. Sano (Eds.), Hybrid Hierarchical Compos. Mater., Springer International Publishing, Cham, 2015, pp. 287–318, https://doi.org/10.1007/978-3-319-12868-9_8.
[12] R.O. Ritchie, The conflicts between strength and toughness, Nat. Mater. 10 (2011) 817–822, https://doi.org/10.1038/nmat3115.
[13] S. Askarinejad, N. Rahbar, Toughening mechanisms in bioinspired multilayered materials, J. R. Soc. Interface 12 (2014) 20140855, https://doi.org/10.1098/rsif.2014.0855.
[14] H. Kakisawa, T. Sumitomo, The toughening mechanism of nacre and structural materials inspired by nacre, Sci. Technol. Adv. Mater. 12 (2011), 064710, https://doi.org/10.1088/1468-6996/12/6/064710.
[15] F. Narducci, S.T. Pinho, Exploiting nacre-inspired crack deflection mechanisms in CFRP via micro-structural design, Compos. Sci. Technol. 153 (2017) 178–189, https://doi.org/10.1016/j.compscitech.2017.08.023.
[16] F. Barthelat, H. Tang, P. Zavattieri, C. Li, H. Espinosa, On the mechanics of mother-of-pearl: a key feature in the material hierarchical structure, J. Mech. Phys. Solid. 55 (2007) 306–337, https://doi.org/10.1016/j.jmps.2006.07.007.
[17] G. Czél, M. Jalalvand, M.R. Wisnom, Demonstration of pseudo-ductility in unidirectional hybrid composites made of discontinuous carbon/epoxy and continuous glass/epoxy plies, Composer Part Appl. Sci. Manuf. 72 (2015) 75–84, https://doi.org/10.1016/j.compositesa.2015.01.019.
[18] G. Czél, S. Pimenta, M.R. Wisnom, P. Robinson, Demonstration of pseudo-ductility in unidirectional discontinuous carbon fibre/epoxy prepreg composites, Compos. Sci. Technol. 106 (2015) 110–119, https://doi.org/10.1016/j.compscitech.2014.10.022.
[19] J. Henry, S. Pimenta, Increasing damage tolerance in composites using hierarchical brick-and-mortar microstructures, J. Mech. Phys. Solid. 118 (2018) 322–340, https://doi.org/10.1016/j.jmps.2018.06.003.
[20] F. Narducci, S.T. Pinho, Interaction between nacre-like CFRP mesolayers and long-fibre interlayers, Compos. Struct. 200 (2018) 921–928, https://doi.org/10.1016/j.compstruct.2018.05.103.
[21] F. Narducci, K.-Y. Lee, S.T. Pinho, Realising damage-tolerant nacre-inspired CFRP, J. Mech. Phys. Solid. 116 (2018) 391–402, https://doi.org/10.1016/j.jmps.2018.04.004.
[22] G. Bullegas, S.T. Pinho, S. Pimenta, Engineering the translaminar fracture behaviour of thin-ply composites, Compos. Sci. Technol. 131 (2016) 110–122, https://doi.org/10.1016/j.compscitech.2016.06.002.
[23] R. Häsä, S.T. Pinho, Failure mechanisms of biological crossed-lamellar microstructures applied to synthetic high-performance fibre-reinforced composites, J. Mech. Phys. Solid. 125 (2019) 53–73.
[24] L.K. Grunenfelder, N. Suksangpanya, C. Salinas, G. Milliron, N. Yaraghi, S. Herrera, K. Evans-Lutterodt, S.R. Nutt, P. Zavattieri, D. Kisailus, Bio-inspired impact-resistant composites, Acta Biomater. 10 (2014) 3997–4008, https://doi.org/10.1016/j.actbio.2014.03.022.
[25] D. Ginzburg, F. Pinto, O. Iervolino, M. Meo, Damage tolerance of bio-inspired helicoidal composites under low velocity impact, Compos. Struct. 161 (2017) 187–203, https://doi.org/10.1016/j.compstruct.2016.10.097.
[26] L. Mencattelli, S.T. Pinho, Realising bio-inspired impact damage-tolerant thin-ply CFRP Bouligand structures via promoting diffused sub-critical helicoidal damage, Compos. Sci. Technol. 182 (2019) 107684, https://doi.org/10.1016/j.compscitech.2019.107684.
[27] V. Rodríguez-García, R. Guzman de Villoria, Automated manufacturing of bio-inspired carbon-fibre reinforced polymers, Compos. B Eng. 215 (2021), https://doi.org/10.1016/j.compositesb.2021.108795, 108795.
[28] HexPly® 8552 Epoxy Matrix (180°C/356°F Curing Matrix) Hexcel Product Data Sheet, (n.d.).
[29] ASTM D5528-01 - Standard Test Method for Mode I Interlaminar Fracture Toughness of Unidirectional Fiber-Reinforced Polymer Matrix Composites, (n.d.).
[30] S.S. Wicks, R.G. de Villoria, B.L. Wardle, Interlaminar and intralaminar reinforcement of composite laminates with aligned carbon nanotubes, Compos. Sci. Technol. 70 (2010) 20–28, https://doi.org/10.1016/j.compscitech.2009.09.001.
[31] ASTM D7905/D7905M - Standard test method for determination of the mode II interlaminar fracture toughness of unidirectional fiber-reinforced polymer matrix composites, (n.d.). http://www.astm.org/cgi-bin/resolver.cgi?D7905D7905M-14 (accessed October 30, 2020).
[32] Z. Yang, C.T. Sun, Interlaminar fracture toughness of a graphite/epoxy multidirectional Composite1, J. Eng. Mater. Technol. 122 (2000) 428–433, https://doi.org/10.1115/1.1289027.
[33] R.H. Martin, Interlaminar Fracture Characterization: a Current Review, NASA, 1991.
[34] E. Zile, V. Tamuzs, Mode II delamination of a unidirectional carbon fiber/epoxy composite in four-point bend end-notched flexure tests, Mech. Compos. Mater. 41 (2005) 383–390, https://doi.org/10.1007/s11029-005-0064-2.
[35] M.-S. Sohn, X.-Z. Hu, Mode II delamination toughness of carbon-fibre/epoxy composites with chopped Kevlar fibre reinforcement, Compos. Sci. Technol. 52 (1994) 439–448, https://doi.org/10.1016/0266-3538(94)90179-1.
[36] S.T. Pinho, P. Robinson, L. Iannucci, Fracture toughness of the tensile and compressive fibre failure modes in laminated composites, Compos. Sci. Technol. 66 (2006) 2069–2079, https://doi.org/10.1016/j.compscitech.2005.12.023.
[37] A. García-Carpintero, B.N.G. van den Beuken, S. Haldar, M. Herráez, C. González, C.S. Lopes, Fracture behaviour of triaxial braided composites and its simulation using a multi-material shell modelling approach, Eng. Fract. Mech. 188 (2018) 268–286, https://doi.org/10.1016/j.engfracmech.2017.08.034.
[38] F. Xiao, C.-Y. Hui, E.J. Kramer, Analysis of a mixed mode fracture specimen: the asymmetric double cantilever beam, J. Mater. Sci. 28 (1993) 5620–5629, https://doi.org/10.1007/BF00367838.
[39] V. Mollón, J. Bonhomme, J. Viña, A. Argüelles, Mixed mode fracture toughness: an empirical formulation for determination in asymmetric DCB specimens, Eng. Struct. 32 (2010) 3699–3703, https://doi.org/10.1016/j.engstruct.2010.08.014.
[40] S. Bennati, M. Colleluori, D. Corigliano, P.S. Valvo, An enhanced beam-theory model of the asymmetric double cantilever beam (ADCB) test for composite laminates, Compos. Sci. Technol. 69 (2009) 1735–1745, https://doi.org/10.1016/j.compscitech.2009.01.019.

[41] A. Arrese, N. Carbajal, G. Vargas, F. Mujika, A new method for determining mode II R-curve by the End-Notched Flexure test, Eng. Fract. Mech. 77 (2010) 51–70, https://doi.org/10.1016/j.engfracmech.2009.09.008.
[42] P.S. Valvo, The effects of shear on mode II delamination, Frat. Ed. Integrità Strutt. 12 (2018) 123–139, https://doi.org/10.3221/IGF-ESIS.44.10.
[43] V. Sundararaman, B.D. Davidson, An unsymmetric end-notched flexure test for interfacial fracture toughness determination, Eng. Fract. Mech. 60 (1998) 361–377, https://doi.org/10.1016/S0013-7944(98)00017-4.
[44] ASTM E399−12 - Standard Test Method for Linear-Elastic Plane-Strain Fracture Toughness KIc of Metallic Materials, (n.d.).
[45] M.J. Laffan, S.T. Pinho, P. Robinson, L. Iannucci, Measurement of the in situ ply fracture toughness associated with mode I fibre tensile failure in FRP. Part II: size and lay-up effects, Compos. Sci. Technol. 70 (2010) 606–613, https://doi.org/10.1016/j.compscitech.2009.12.016.
[46] M.J. Laffan, S.T. Pinho, P. Robinson, A.J. McMillan, Translaminar fracture toughness testing of composites: a review, Polym. Test. 31 (2012) 481–489, https://doi.org/10.1016/j.polymertesting.2012.01.002.
[47] L.J. Bonderer, A.R. Studart, L.J. Gauckler, Bioinspired design and assembly of platelet reinforced polymer films, Sci. New Ser. 319 (2008) 1069–1073.
[48] D. Carnelli, R. Libanori, T.P. Niebel, A.R. Studart, Artificially roughened microplatelets for high- performance bioinspired composites, in: ECCM17, 2016. Munich, Germany.
[49] Z. Yin, F. Hannard, F. Barthelat, Impact-resistant nacre-like transparent materials, Mater. Sci. 364 (2019) 1260–1263.
[50] D.V. Wilbrink, M. Utz, R.O. Ritchie, M.R. Begley, Scaling of strength and ductility in bioinspired brick and mortar composites, Appl. Phys. Lett. 97 (2010) 193701, https://doi.org/10.1063/1.3499294.
[51] J.M. Whitney, C.E. Browning, W. Hoogsteden, A double cantilever beam test for characterizing mode I delamination of composite materials, J. Reinforc. Plast. Compos. 1 (1982) 297–313, https://doi.org/10.1177/073168448200100402.
[52] A.J. Smiley, R.B. Pipes, Rate effects on mode I interlaminar fracture toughness in composite materials, J. Compos. Mater. 21 (1987) 670–687, https://doi.org/10.1177/002199838702100706.
[53] R. Rikards, F.-G. Buchholz, A.K. Bledzki, G. Wacker, A. Korjakin, Mode I, mode II, and mixed-mode I/II interlaminar fracture toughness of GFRP influenced by fiber surface treatment, Mech. Compos. Mater. 32 (1996) 439–462, https://doi.org/10.1007/BF02313863.
[54] J.M. Whitney, Chapter 4 - experimental characterization of delamination fracture, in: Interlaminar Response Compos. Mater., 1989, pp. 161–250.
[55] L.A. Carlsson, J.W. Gillespie, R.B. Pipes, On the analysis and design of the end notched flexure (ENF) specimen for mode II testing, J. Compos. Mater. 20 (1986) 594–604, https://doi.org/10.1177/002199838602000606.
[56] S. Hashemi, A.J. Kinloch, J.G. Williams, The analysis of interlaminar fracture in uniaxial fibre-polymer composites, Proc. Roy. Soc. Lond. 427 (1990) 173–199, https://doi.org/10.1098/rspa.1990.0007.
[57] J.A. Nairn, Analytical and Numerical Modeling of R Curves for Cracks with Bridging Zones, (n.d.) 20.
[58] E.S. Greenhalgh, Failure Analysis and Fractography of Polymer Composites, Woodhead Publishing Limited, 2009.
[59] E.S. Greenhaigh, Characterisation of Mixed-Mode Delamination Growth in Carbon-Fibre Composites, Imperial College of Science, Technology and Medicine, 1998.
[60] M. Yasaee, I.P. Bond, R.S. Trask, E.S. Greenhalgh, Mode I interfacial toughening through discontinuous interleaves for damage suppression and control, Composer Part Appl. Sci. Manuf. 43 (2012) 198–207, https://doi.org/10.1016/j.compositesa.2011.10.009.
[61] C.J. Norris, R.S. Trask, I.P. Bond, Interactions between propagating cracks and bioinspired self-healing vascules embedded in glass fibre reinforced composites, Compos. Sci. Technol. 71 (6) (2011) 847–853, https://doi.org/10.1016/j.compscitech.2011.01.027.
[62] M.A. Meyers, P.-Y. Chen, A.Y.-M. Lin, Y. Seki, Biological materials: structure and mechanical properties, Prog. Mater. Sci. 53 (2008) 1–206, https://doi.org/10.1016/j.pmatsci.2007.05.002.
[63] F. Narducci, S.T. Pinho, Interface micro-texturing for interlaminar toughness tailoring: a film-casting technique, Compos. Sci. Technol. 156 (2018) 203–214, https://doi.org/10.1016/j.compscitech.2017.10.016.
[64] F. Libonati, A.E. Vellwock, F. Ielmini, D. Abliz, G. Ziegmann, L. Vergani, Bone-inspired enhanced fracture toughness of de novo fiber reinforced composites, Sci. Rep. 9 (2019) 3142, https://doi.org/10.1038/s41598-019-39030-7.
[65] M.E. Launey, R.O. Ritchie, On the fracture toughness of advanced materials, Adv. Mater. 21 (2009) 2103–2110, https://doi.org/10.1002/adma.200803322.
[66] P.D. Mangalgiri, W.S. Johnson, R.A. Everett, Effect of Adherend Thickness and Mixed Mode Loading on Debond Growth in Adhesively Bonded Composite Joints, NASA, 1986.
[67] F. Ducept, A mixed-mode failure criterion derived from tests on symmetric and asymmetric specimens, Compos. Sci. Technol. 59 (1999) 609–619, https://doi.org/10.1016/S0266-3538(98)00105-5.
[68] V. Sundararaman, B.D. Davidson, An unsymmetric double cantilever beam test for interfacial fracture toughness determination, J. Solids Struct. 34 (1997) 799–817.
[69] D. Purslow, Matrix fractography of fibre-reinforced epoxy composites, Composites 17 (1986) 289–303, https://doi.org/10.1016/0010-4361(86)90746-9.
[70] M. Herráez, N. Pichler, J. Botsis, Improving delamination resistance through tailored defects, Compos. Struct. 247 (2020) 112422, https://doi.org/10.1016/j.compstruct.2020.112422.
[71] H. Albertsen, J. Ivenqh, P. Peters, M. Wevers, I. Verpoest, Interlaminar fracture toughness of CFRP influenced by fibre surface treatment: Part 1. Experimental results, Compos. Sci. Technol. 54 (1995) 133–145.
[72] HexTow® AS4 Carbon Fiber. Hexcel Product Datasheet, (n.d.).
[73] M. Herráez, A.C. Bergan, C. González, C.S. Lopes, Modeling Fiber Kinking at the Microscale and Mesoscale, NASA, 2018.
[74] S. Pimenta, S.T. Pinho, An analytical model for the translaminar fracture toughness of fibre composites with stochastic quasi-fractal fracture surfaces, J. Mech. Phys. Solid. 66 (2014) 78–102, https://doi.org/10.1016/j.jmps.2014.02.001.
[75] G. Bullegas, J. Benoliel, P.L. Fenelli, S.T. Pinho, S. Pimenta, Towards quasi isotropic laminates with engineered fracture behaviour for industrial applications, Compos. Sci. Technol. 165 (2018) 290–306, https://doi.org/10.1016/j.compscitech.2018.07.004.